A diffuse interface method for solid-phase modeling of regression behavior in solid composite propellants

Baburaj Kanagarajan, J. Matt Quinlan, Brandon Runnels*

Department of Mechanical and Aerospace Engineering, University of Colorado, Colorado Springs, CO USA

Abstract

Solid composite propellants (SCPs) are ubiquitous in the field of propulsion. In order to design and control solid rocket motors, it is critical to understand and accurately predict SCP regression. Regression of the burn surface is a complex process resulting from thermo-chemical-mechanical interactions, often exhibiting extreme morphological changes and topological transitions. Diffuse interface methods, such as phase field (PF), are well-suited for modeling processes of this type, and offer some distinct numerical advantages over their sharp-interface counterparts. They also provide a convenient framework for incorporating multiple multiphysical dynamics. In this work, we present a phase-field method for modeling the regression of SCPs with varying species and geometry. We construct the model from a thermodynamic perspective, leaving the base formulation general. A diffuse-species-interface field is employed as a mechanism for capturing complex burn chemistry in a reduced-order fashion, making it possible to model regression from the solid phase only. The computational implementation, which uses block-structured adaptive mesh refinement and temporal substepping for increased performance, is briefly discussed. The model is then applied to four test cases: (i) pure AP monopropellant, (ii) AP/PBAN sandwich, (iii) AP/HTPB sandwich, and (iv) spherical AP particles packed in HTPB matrix in two and three dimensions. In all cases, reasonable quantitative agreement is observed, even when the model is applied predictively (i.e., no parameter adjustment), as in the case of (iv). The validation of the proposed PF model demonstrates its efficacy as a numerical design tool for future SCP investigation.

Keywords: Solid composite propellants, Numerical simulation, Phase field modeling, Diffuse interface methods

1. Introduction

Solid composite propellants (SCPs) are composed of a mixture of fuel and oxidizer species that are unmixed at the molecular level. An example of a modern SCP oxidizer/fuel combination is ammonium perchlorate (AP) particles in a hydroxyl-terminated polybutadiene (HTPB) matrix. SCPs such as this have become the propellant of choice in the field of solid rocket propulsion for tactical missiles and launch vehicle

*Corresponding author
Email address: brunnels@uccs.edu (Brandon Runnels)

boosters. Even though SCPs have slightly lower performance than complex liquid rocket engines, they are simple, reliable and chemically/mechanically stable in long-term storage.

In solid rocket motors the burn rate and its dependence on the gas dynamic ballistics is a critical variable for a number of reasons. First, the burn rate and grain surface area determine the propellant flow rate and, as a result, the motor thrust. Second, how the burn rate is changed by the local pressure and flow near the burning surface is an important factor in preventing combustion instabilities. The burn rate is a function of the properties of the solid components and their mass fractions, enthalpies of phase change, chemical reaction mechanism, flame structures, heat transfer mechanisms, and internal ballistic gas dynamics. Specifically, the most important parameters are the AP mass fraction and the AP particle sizes [1]. An extensive set of experiments varying the particle size and concentration of AP on the burning rate was performed by Bastress [2]. While there have been numerous experimental measurements of SCP burn rates, many of the details of the combustion and detailed solid-fluid interaction remain unknown.

One of the confounding issues is the complex combustion mechanism. In addition to being an oxidizer, pure AP can support a self deflagration wave, for which the burn rates have been measured [3–7]. On the other hand, the fuel/binders cannot act as a monopropellant, rather, heat transfer from the gas-phase reactions causes the long polymer chains of the binder to pyrolyze and sublimate into mainly shorter chain hydrocarbons. When AP particles are suspended in a matrix of binder such as HTPB or polybutadiene acrylonitrile (PBAN) the resulting flame structure is complex and unsteady, which makes the experimental burn rate measurement challenging. Despite this, a substantial amount of of historical data has been gathered over the past several decades [8, 9]. The two most common methods for measuring the burn rate are with break-wires [10] or optically [9, 11–14]. Experimental investigation of sandwich structures has made it possible to distill the binder/oxidizer interactions in a simple yet nontrivial SCP geometry. For instance, the burn rates have been measured in a composite structure made of a single layer of binder sandwiched between two layers of pure AP [4, 15, 16]. These data can be used to validate numerical burn rate models.

There are several numerical models that have been developed to estimate the burn rate. A simple steady-state combustion of SCPs was developed as a two parameter, power law in pressure $r = a(P/P_0)^n$ [17]. Even though this model fails to capture important features such as the relation between the unsteady flame structure and the burning rate, it remains very useful. Another model was developed that introduces a mechanism to drive the energy release at the burning surface and the heterogeneous reaction of the oxidizer [18]. The next increase in model complexity comes by considering the flame structure. For instance, models have been introduced where the assumed structure is three flames instead of one: (a) premixed binder rich flame, (b) lean premixed oxidizer (AP) flame, and (c) the diffusion flame anchored by the other two premixed flames [19–21]. The relation between flame structure and burn rate calculations in modeling has been extensively studied [22–24]. In some gas-phase models, erosive burning near the surface of the propellant have been incorporated into a three-flame model to include the effect of the high-velocity gas flow [25, 26]. Since real SCPs are have a wide distribution of AP particle sizes, models have been created to

include a bimodal distribution of AP particles, for instance, the petite ensemble model, which also includes the temperature sensitivity of the SCP [27]. An analytical method based on pressure and temperature correlation has been developed to study the dependence of SCP deflagration rate on pressure and initial temperature [28] for SCPs. One of the key findings experimentally was that the burning rates of the AP composite propellants increase with increasing AP concentration and decreasing AP diameter [29]—a finding that is supported with current modeling efforts [30].

Experimental observation indicates that the burn surface is far from planar [31]. In general, material heterogeneity produces a highly complex burn front, sometimes producing particles of polymer binder or oxidizer that are advected away by the flow [32]. To model this behavior, it is necessary to adopt a numerical approach capable of resolving complex geometry and topological transitions. Explicit meshing of the regressing surface is cumbersome and can be prohibitively difficult, especially when topological transitions occur. Eulerian approaches, in which the interface moves through the grid, are more attractive. Two such methods, both treating the interface as a sharp discontinuity, have been predominantly used to study regression. The first, originally proposed by Hegeb et al. [33] and since applied by Massa et al., [34] and others [35], is to use a coordinate transformation to map the regressing surface to a planar surface. Although this works well for near-planar surfaces, it can fail when the surface experiences a topological transition, which can make it impossible to construct a smooth map. The second is to use the level-set (LS) method, which relies on the evolution of a surrogate field, an isocontours of which may be regarded as a sharp surface. This was originally applied by Wang et al. [36] and others [37, 38] to modeling surface regression in SCPs. Here, surface regression is effected by the calculated local regression rate, which is used to update the surrogate field and then a new interface is approximated by the updated isocontour. While sharp interface methods are often desirable due to their increased accuracy, we suggest that the problem of interface regression does not particularly benefit from this enhanced precision due to the lack of sharpness in the physical interface itself. As such, some of the cumbersome numerical tasks needed for sharp interfaces (front tracking, explicit boundary conditions, nondifferentiability, etc.) needlessly complicate the solution.

In this work, we present a diffuse interface model for surface regression. Here the solid/gas phase transition is treated as continuous at very small scales. The phase field (PF) model provides an attractive framework for modeling combustion [39–41] using a Gibbs-type construction. It also provides an elegant means for tracking complex surface evolution by modeling interfaces as diffuse. PF models have been employed in a wide range of settings including microstructure evolution [42–44], fracture mechanics [45, 46], dendritic growth [47], and solid-fluid interactions [48–50]. PF provides a robust means for thermodynamic modeling of combined multiphysics processes, while retaining the ability to capture complex morphological behavior. It also provides interpretability to model parameters (e.g., order parameter as a reaction coordinate, chemical potential as a reaction energy, diffuse boundary as a reaction zone, etc.). Indeed, the great advantage of the phase field method is the ease with which it can be extended to treat fully complex fluid phase phenomena (mixing, diffusion, and reactions) as well as solid phase behavior (thermal and elastic response). In this

work, the scope is restricted to burn rate prediction based on ambient pressure only using a heuristic rate law, and does not include concurrent simulation of fluid or solid phase mechanics. It is entirely possible, though, to couple this present model to both solid and fluid phase models, replacing the heuristic rate law with fully resolved solid and gas dynamics. (We refer the reader to concurrent work [51], which directly addresses the challenges of solid/fluid coupling in diffuse boundary models.)

The PF can caues a substantial increase in the computational resolution necessary to resolve the solution across the diffuse boundary. Through the strategic application of meshing techniques like local adaptive mesh refinement, however, it is possible to achieve good performance with sufficiently high accuracy.

The remainder of the paper is structured as follows: In Section 2 we develop the chemical and thermodynamic description of the phase field solid propellant burn model, the derivation of the burn speed from the model, and the incorporation of multi-species effects though a diffuse species parameter. The presented model, like most diffuse interface methods, requires the application of specialized computational techniques to solve in a tractable manner. Therefore, in Section 3, we briefly discuss the computational framework that is used to implement the model and generate results. In Section 4, we examine four distinct cases: pure AP, AP with a thin "sandwich" laminate of PBAN, AP with a thin "sandwich" laminate of HTPB, and packed AP spheres in an HTPB matrix. The first three cases are used to calibrate our model, which is then applied to the practical example of packed AP spheres in an HTPB matrix in two and three dimensions. In all of these cases, we demonstrate the efficacy of the model via comparison to legacy experimental data. We conclude this work in Section 5 with a discussion synthesizing results and the limitations of the model. This section also outlines the path forward for integrating other physical dynamics into the proposed framework.

2. Phase field solid burn model

In this section we present the phase field model as applied to the problem of SCPs. Consider a continuum region Ω filled with burned or unburned SCP. Ω is generally uninteresting, and is in practice often a rectilinear computational domain, as the geometry of the solid phase is resolved implicitly (Fig. 1, left and center). Over this region we define a field variable, commonly referred to as an order parameter $\eta : \Omega \to [0, 1]$. Physically, η may be regarded as a pointwise reaction coordinate that tracks the progress of the burn reaction as a function of space and time. In this work we regard the problem as being two-phase, considering solid and fluid only; that is, no melting is considered. It is important to note that in a case with more species or phases, η can no longer be interpreted as a reaction coordinate and should be replaced with an alternative construction such as a set of volume or mole fractions.

The order parameter functions simultaneously as a thermodynamic reaction coordinate and an indicator function describing the geometry of the unburned region. We now begin our construction of a phase field model through the establishment of a free energy functional $f : C_2(\Omega, [0, 1]) \to \mathbb{R}$, given by,

$$f[\eta] = \int_\Omega \left[\lambda w(\eta) + \frac{1}{2}\varepsilon^2 \kappa |\nabla \eta|^2 \right] \, \mathrm{d}\boldsymbol{x}, \tag{1}$$

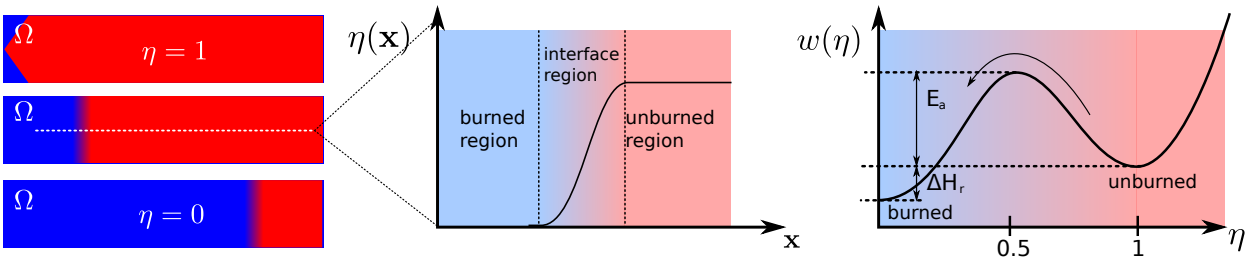

Figure 1: The order parameter η representations—(a) Order parameter $\eta = 1$ shows unburned region, $\eta = 0$ shows the burned region and the interface region is $0 < \eta < 1$, (b) The representation of order parameter η in terms of burned, unburned and interface regions along the length of the coupon, (c) The representation of free energy $w(\eta)$ in terms of burned, unburned and interface regions

where the square brackets on f should be understood to indicate dependencies on the enclosed arguments and their spatial/temporal derivatives. Normal invariant notation (∇ indicates the gradient, Δ the Laplacian, etc.) is employed. The first term in the integrand indicates the chemical potential, w, which is generally a differentiable multiwell function with minima at 0 and 1 (Fig. 1, right). The coefficient λ is, for practical purposes, a scaling factor, but also admits interpretation as a Lagrange multiplier that may be scaled arbitrarily to bring the solution close to the sharp interface limit. The second term in the integrand introduces nonlocality by penalizing gradients in η. The coefficient κ can be interpreted as the energy of the interface (i.e., surface tension) between the burned and unburned region; here, we simply view it as a numerical regularization. The variable ε, then, is a parameter that controls the length scale of the solution, and will be discussed in more detail subsequently.

The free energy functional f provides the basis for the construction of a kinetic evolution equation. We adopt the classical *ansatz*, following non-equilibrium thermodynamic theory as well as the classical Ginzburg-Landau theory [52] that the order parameter evolves proportionally to the gradient of the free energy. A kinetic variable, called the "mobility" (L) is used scale the flow of η. As will be shown subsequently, dividing by the length scale ε is necessary to prevent dependence of the flame speed on the numerical interface region width. The equation governing the evolution is given by the following:

$$\frac{\partial \eta}{\partial t} = -\frac{L}{\varepsilon}\frac{\delta f}{\delta \eta} = -L\left[\frac{\lambda}{\varepsilon}\frac{\partial w}{\partial \eta} - \varepsilon\kappa\Delta\eta\right], \tag{2}$$

where $\delta/\delta\eta$ is the variational derivative. The relatively low order of Eq. (2) makes it readily solvable using optimized explicit methods, as discussed in Section 3. Coupling to additional physics occurs through the modification of Eq. (1) to include other thermodynamic contributions such as thermal or elastic free energies, which are then integrated into the governing equation through the variational derivative. As we will show, however, the reactive and diffusive components alone suffice to capture a broad range of SCP behavior.

2.1. Determining burn rate in the limit

Of particular interest in this present work is the connection of the governing equation to the burn rate in the sharp-interface limit. To begin, we derive the relationship between one-dimensional burn rate and model

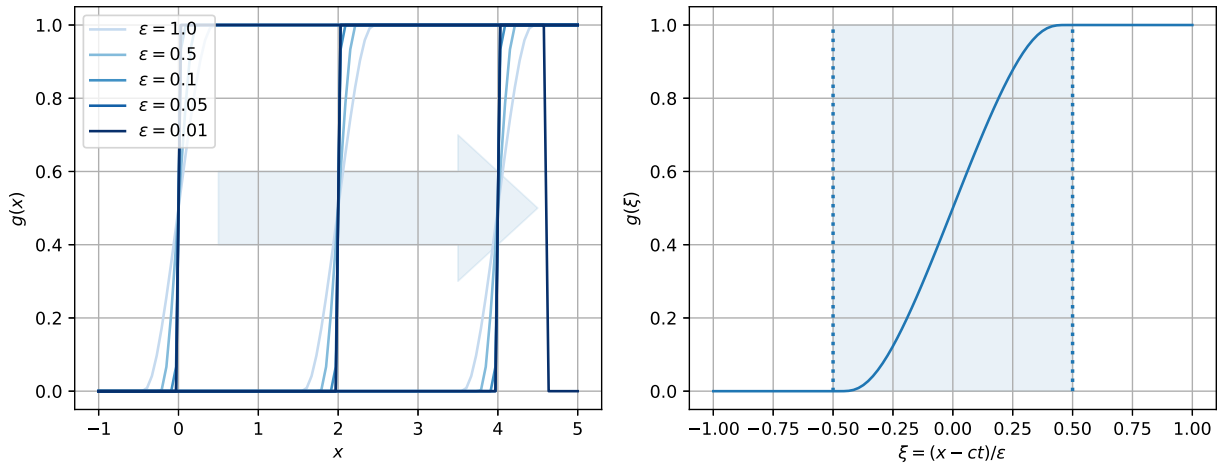

Figure 2: Illustration of 1D burn rate calculation. Diffuse interface converges to the sharp interface limit as $\varepsilon \to 0$, and the interface moves from left to right at a constant velocity c (left). All functions can be collapsed onto a single function $g(\xi)$, where the derivative is nonzero only in the shaded $(-\epsilon/2, \epsilon/2)$ region (right).

parameters in a single-species material, in order to interpret the model parameters (L, ε, etc) in terms of measurable properties. (We comment that the proof presented in this section, though important, is fairly technical. If desired, the reader may skip to the salient result, Eq. (9), without a loss of continuity.) For the case of steady burning, we approximate

$$\eta_\varepsilon(x,t) = g(\xi) \qquad\qquad \xi = \frac{x - ct}{\varepsilon}, \tag{3}$$

where g is a monotonically increasing C_2 function satisfying: (1) $g(\xi) = 0$, $g'(\xi) = 0$ when $\xi \leq -\varepsilon/2$; (2) $g(\xi) = 1$, $g'(\xi) = 0$ when $\xi \geq \varepsilon/2$; (3) antisymmetry of $g(\xi) - \frac{1}{2}$ about $\xi = 0$ (Fig. 2). The constant c is the rate of regression, which will be solved for here. We do not currently specify any limits on ε, but will show that the solution satisfies the governing equations and scales with ε. Now, substituting into the governing equation produces

$$-\frac{c}{\varepsilon}\frac{\mathrm{d}g}{\mathrm{d}\xi} = -L\Big[\frac{\lambda}{\varepsilon}\frac{\mathrm{d}w}{\mathrm{d}g} - \frac{\kappa}{\varepsilon}\frac{\mathrm{d}^2 g}{\mathrm{d}x^2}\Big]. \tag{4}$$

The nonlinearity induced by the chemical potential renders Eq. (4) unsolvable in the general case, which is undesirable as we seek a general relationship between the chemical potential, mobility, and burn width. Therefore we seek a solution in the weak form by integrating both sides over the region $[-\varepsilon/2, \varepsilon/2]$:

$$c\int_{-\varepsilon/2}^{\varepsilon/2} \frac{\mathrm{d}g}{\mathrm{d}\xi}\,\mathrm{d}\xi + L\kappa\int_{-\varepsilon/2}^{\varepsilon/2} \frac{\mathrm{d}^2 g}{\mathrm{d}x^2}\,\mathrm{d}\xi = L\int_{-\varepsilon/2}^{\varepsilon/2} \frac{\mathrm{d}w}{\mathrm{d}g}\,\mathrm{d}\xi. \tag{5}$$

By inspection, and application of the properties of g, we find that the first integral reduces to unity, and the second to zero. Next, applying a change of basis, the integral on the right-hand side becomes

$$\int_0^1 \frac{\mathrm{d}w}{\mathrm{d}g}\frac{\mathrm{d}\xi}{\mathrm{d}g}\,\mathrm{d}g. \tag{6}$$

From this we derive the first important result, that flame speed c does not depend on the barrier height (activation energy) of w. The proof of this follows by noting that w can be additively decomposed into two functions that are symmetric and antisymmetric about $g = 0.5$; $w(g) = w_s(g) + w_a(g)$. Barrier height will generally contribute to w_s but not to w_a. Because w_s is symmetric, it then follows that $\mathrm{d}w_s/\,\mathrm{d}g$ is antisymmetric about $g = 0.5$. Recalling that $g - 0.5$ is antisymmetric about $g = 0.5$, we see that $\mathrm{d}\xi/\,\mathrm{d}g$ is symmetric, and consequently

$$\int_0^1 \frac{\mathrm{d}w_s}{\mathrm{d}g}\frac{\mathrm{d}\xi}{\mathrm{d}g}\,\mathrm{d}g = 0, \tag{7}$$

concluding the proof of the above result. Since the speed depends on the antisymmetric part of the chemical potential only, we can re-write it in terms of a template function $\hat{w}_a$ where $\hat{w}_a(0) = 0, \hat{w}_a(1) = 1$ so that

$$w = w_0 + (w_1 - w_0)\hat{w}_a + w_{1/2}w_s \tag{8}$$

where w_0, w_1, and $w_{1/2}$ are parameters that can be calibrated for the material. This leads finally to the relation

$$c = \lambda L(w_1 - w_0)\gamma[\hat{w}_a], \tag{9}$$

where γ is a constant determined by evaluating Eq. (6) for the choice of template function. From this we see that, in the one-dimensional case, the mobility is proportional to the regression rate divided by the energy difference associated with the reaction. As $\varepsilon \to 0$, we obtain the sharp interface limit, for which the above analysis shows the one-dimensional case to be unchanged. As the diffuse thickness goes to zero, the interface at any point can be approximated as planar (due to the C_2 restriction on η) within a sufficiently small neighborhood, allowing the interface motion at all points to be regarded locally as one-dimensional. Therefore, we conclude that Eq. (9) holds as a general statement of the relation between speed and mobility in the sharp-interface limit.

2.2. Chemical potential specialization

We showed in the previous section that the behavior of the model is insensitive to the precise choice of chemical potential w (up to scaling), and is in fact impervious to the magnitude of the energy barrier.

Therefore we adopt, for convenience, a polynomial approximation to w:

$$w(\mathbf{x}, \eta) = \sum_{i=1}^{N} a_i(\mathbf{x})\, \eta^i(\boldsymbol{x}). \tag{10}$$

Proper segregation of the solution to $\eta = 0$ and $\eta = 1$ requires that $w(0)$ and $w(1)$ be stable local equilibria. To capture the energy of the reaction, the chemical energy at those two points (w_0, w_1, respectively) must be specified. Finally, an energy barrier must be prescribed as well ($w_{1/2}$). Consequently, a suitable polynomial must satisfy the following conditions:

$$w(0) = w_0 \qquad \frac{\partial w}{\partial \eta}\Big|_{\eta=0} = 0 \qquad w_{1/2} = w(1/2) \qquad w(1) = w_1 \qquad \frac{\partial w}{\partial \eta}\Big|_{\eta=1} = 0. \tag{11}$$

In order to satisfy the above conditions, w must be of degree four (having five coefficients) or greater. A fourth order polynomial is used here for simplicity, and because it has been shown to work well for other models of this type (see, for instance, [53, 54]). Solving the above equations for $a_0, \ldots, a_4$ produces

$$\begin{bmatrix} a_0 \\ a_1 \\ a_2 \\ a_3 \\ a_4 \end{bmatrix} = \begin{bmatrix} 1 & 0 & 0 \\ 0 & 0 & 0 \\ -11 & 16 & -5 \\ 18 & -32 & 14 \\ -8 & 16 & -8 \end{bmatrix} \begin{bmatrix} w_0 \\ w_{1/2} \\ w_1 \end{bmatrix}. \tag{12}$$

It is possible to tailor w to a form that is informed by the chemistry, in which the form of w corresponds to the reaction energy as a function of reaction coordinate η. It is also possible to extend this potential to capture multi-phase (solid/liquid/gas) behavior through the addition of another minima at a value of η designated to be a liquid phase. In this work, the aim is to show the efficacy of a simple model in capturing regression rates; these extensions will be considered in future work.

2.3. Mobility calculation

In composite propellants, multiple constituent species interact chemically to sustain deflagration in the thermodynamic regime of interest. Ammonium perchlorate will burn as a monopropellant, whereas fuel binders (HTPB/PBAN) decompose but do not burn on their own [55]. Therefore a regression rate model must capture the effect of the species concentration and spatial distribution on regression rate. We introduce a spatial variable, called the diffuse species field ($\phi(\boldsymbol{x}, t)$) to determine pointwise concentration of oxidizer and binder. We adopt the convention that $\phi = 1$ corresponds to pure oxidizer, $\phi = 0$ to pure binder. In principle, ϕ can be evolved in time to represent morphological changes (such as agglomeration of particles) during the burn. In this work, however, the diffuse species field does not evolve in time. It is defined at all times and for both the burned and unburned regions. The purpose of ϕ is to determine material-specific properties (like mobility) that are used to evolve η, and it is generally prescribed as an initial condition.

Material characteristics can then be represented simply using a mixture rule. (Note that the use of a mixture rule is not to effect *homogenization*, but rather to allow a smooth transition between material types

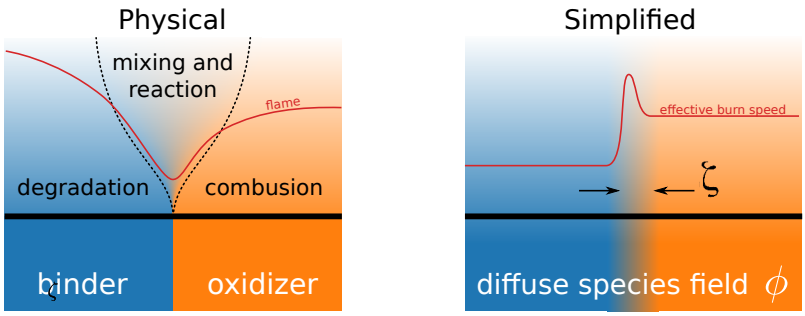

Figure 3: Schematic illustrating the concept of the diffuse species concentration simplification. (Left: Physical) At the boundary, binder and oxidizer diffuse and mix at the species boundary, which enables combustion to occur. Far from the boundary, the binder degrades and the oxidizer burns, and the result is a flame that is close to the solid interface near the species boundary, but further away from the oxidizer interface and even further from the binder interface. Physically this produces differing regression rates in the three regimes of interest. (Right: Simplified) The diffuse species field ϕ is used to adjust the effective regression rate depending on the species—generally, slow in the binder, faster for the oxidizer, and fastest in the interfacial region.

in an explicitly resolved SCP geometry. For a discussion of homogenization, and some of the associated challenges, the reader is directed to [56].) We aim to use continuous material variability to capture the effect of material heterogeneity on regression rate. Physically, this is a consequence of the mass fluxes and diffusion causing mixing and facilitating reactions. The differing local mole fractions that result from the flux from different propellant species cause locally differences in the reaction rate and flame height above the solid. These differences greatly influence the heat fluxes into the solid and hence the regression rate.

Far from the binder/AP boundary, the AP can support a self deflagration flame, which ensures that there is some heat transfer from the flame back to the solid—driving the surface regression. Also far from the interface, but over the binder, any heat fed back to the solid goes to transforming the species and the phase to gaseous fuel species. This is an endothermic process and results in a generally slow binder surface regression. Near the interface, the gaseous fuel and oxidizers have strong gradients and as a consequence diffuse rapidly towards each other. Specifically, a diffusion flame results from the diffusion of fuel and oxidizer together (in stoichiometric proportions) away from the solid surface, because the heat transfer is too fast back to the solid but temperatures are too low for combustion. In other words, the diffusion flame is slightly lifted from the solid surface. This lifted diffusion flame, and the lean/rich premixed flames that sit at the base of the diffusion flame, induce very steep temperature gradients normal to the surface. Since this causes very high heat transfer from the flame to the solid, near the interface, the local regression rate is considerably higher near the solid/solid interface.

To capture this phenomenon, it is necessary to modify the property field in such a way as to capture local interface-specific properties; namely, the pointwise burn rate is

$$L_{\text{eff}}(\boldsymbol{x},t) = L_{\text{bin}}(1-\phi(\boldsymbol{x},t)) + L_{\text{ox}}\phi(\boldsymbol{x},t) + 4\,\phi(\boldsymbol{x},t)\,(1-\phi(\boldsymbol{x},t))L_{\text{int}} \tag{13}$$

where L_{bin} and L_{ox} are the mobility of the pure binder and pure oxidizer, respectively, and L_{int} is an interface mobility correction term. In this way, we capture the effect of interface mixing and reaction chemistry

(Fig. 3 left) using a reduced order surrogate model for pressure-informed burn speed (Fig. 3 right), without incurring the cost of a full gas-phase simulation. The diffusiveness of the species boundary is determined by a parameter, ζ, which controls the degree of mixing of the two species. The individual mobilities are calculated by combining a pressure power law for c with Eq. (9), yielding the expression

$$L_i = \frac{n_i \, (p/p_{pi})^{r_i}}{\lambda \, (w_{1i} - w_{0i})\gamma} \tag{14}$$

where variables with an i subscript take on different values for different regimes (binder, oxidizer, and interface). The constants n_i and r_i are calibrated power law parameters, λ and γ_0 are model constants, p is the pressure, and w_{1i}, w_{0i} are burned and unburned energies, respectively. Values for all parameters and model constants are enumerated in Table 1.

2.4. Summary

We conclude this section by reiterating the essential components of the model, distilling the governing equations, initial conditions (ICs), boundary conditions (BCs), and other equations together in a streamlined presentation. We always assume that simulation time starts at $t = 0$. The solution domain is denoted Ω, and contains two types of boundaries: Dirichlet boundaries ($\partial_1\Omega$) and periodic boundaries. The following is a complete description of the model for the evolution of η:

$$\text{Evolution of } \eta: \quad \frac{\partial \eta}{\partial t} = -L_{\text{eff}}(\boldsymbol{x})\Big[\frac{\lambda}{\varepsilon}\frac{\partial w}{\partial \eta} - \varepsilon\,\kappa\,\Delta\eta\Big] \qquad \forall \boldsymbol{x} \in \Omega,\, t \geq 0 \tag{15a}$$

$$\text{Unburned IC:} \quad \eta(\boldsymbol{x}, 0) = 1.0 \qquad \forall \boldsymbol{x} \in \Omega \tag{15b}$$

$$\text{Dirichlet BC:} \quad \eta(\boldsymbol{x}, t) = \eta_0(\boldsymbol{x}, t) \qquad \forall \boldsymbol{x} \in \partial_1\Omega,\, t \geq 0 \tag{15c}$$

$$\text{Chemical potential:} \quad w(\eta) = \begin{bmatrix} 1 & \eta & \eta^2 & \eta^3 & \eta^4 \end{bmatrix} \begin{bmatrix} 1 & 0 & 0 \\ 0 & 0 & 0 \\ -11 & 16 & -5 \\ 18 & -32 & 14 \\ -8 & 16 & -8 \end{bmatrix} \begin{bmatrix} w_0 \\ w_{1/2} \\ w_1 \end{bmatrix} \qquad \eta \in [0, 1] \tag{15d}$$

$$\text{Diffuse species field:} \quad \phi(\boldsymbol{x}, t) = \phi_0(\boldsymbol{x}) \qquad \forall \boldsymbol{x} \in \Omega,\, t \geq 0 \tag{15e}$$

$$\text{Mobility calculation:} \quad L_{\text{eff}}(\boldsymbol{x}, t) = L_{\text{bin}}\,(1 - \phi(\boldsymbol{x}, t)) + L_{\text{ox}}\,\phi(\boldsymbol{x}, t) + 4\phi(\boldsymbol{x}, t)(1 - \phi(\boldsymbol{x}, t))L_{\text{int}} \qquad \forall \boldsymbol{x} \in \Omega,\, t \geq 0 \tag{15f}$$

$$\text{Pressure power law:} \quad L_i = \frac{n_i (p/p_{0i})^{r_i}}{\lambda (w_{1i} - w_{0i})\gamma} \qquad i = \text{bin}, \text{ox}, \text{int}. \tag{15g}$$

The primary equation to be solved is the reaction-diffusion equation for the evolution of η, Eq. (15a), a nonlinear parabolic partial differential equation. The entire domain is initialized in an unburned state (Eq. (15b)), and burn is initiated through boundary conditions (Eq. (15c)) by setting $\eta_0 = 0$ on the $x_{\min}$ face and $\eta_0 = 1$ on the $x_{\max}$ face. The other faces are periodic. The nonlinearity is introduced by the choice of nonlinear potential w (Eq. (15d)), which is defined through three model parameters $w_0, w_{1/2}, w_1$, corresponding to the burned energy, energy barrier, and unburned energy, respectively. The diffuse species

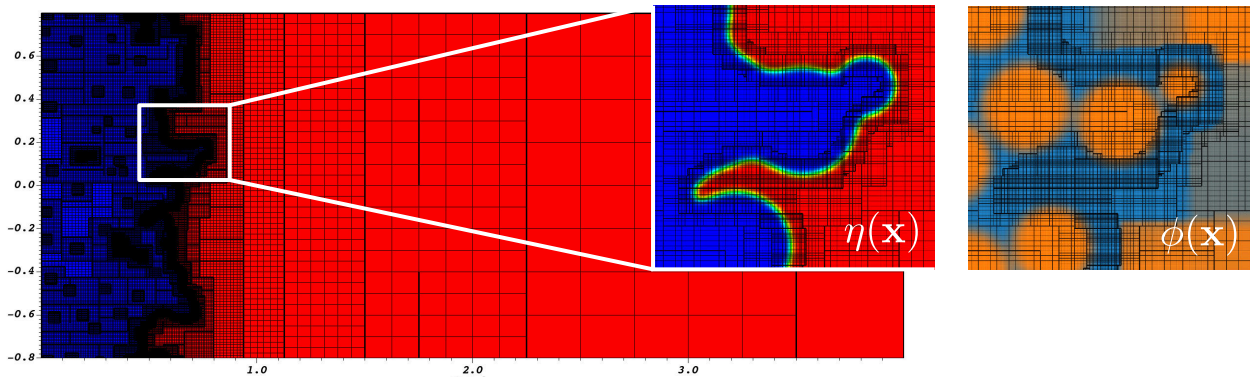

Figure 4: Sample result (from packed spheres case) illustrating the use of block-structured adaptive mesh refinement at the boundary. The base level grid is very coarse (left). Multiple BSAMR levels allows for refinement at the η boundary (left popout). Refinement is based only on η (not on ϕ), and ϕ is updated only on an as-needed basis to enhance performance (right popout).

field is based on a prescribed input $\phi_0(\boldsymbol{x})$ (Eq. (15e)) and is used to calculate the mobility L_{eff} using a mixture law (Eq. (15f)). The mixture law is determined based on individual single-species mobilities as well as an "interface mobility", all of which follow a pressure-dependent power law (Eq. (15g)), with parameters $n_i, p_{0i}, \lambda, \gamma$ given as model inputs. The chemical potential weight λ, interface diffuse width ε, and interface energy parameter κ are all given as model inputs. Because the main governing equation is parabolic, the solution is generally well-behaved for a sufficiently small timestep, and can therefore be solved using basic explicit numerical integration techniques.

We pause here to note the physical phenomena that are not resolved by this model. The model does not explicitly simulate the fluid phase, nor does it include any of the solid-phase mechanics. Instead, the effects of the solid and fluid phase are captured through a reduced order model for the interface mobility, which controls the regression. As will be shown subsequently, it is possible to come close to experimental results even with these simplifications. It is important, however, to emphasize that a key feature of this model is that since it is an energy-based framework and uses a diffuse interface structure, it is easy to incorporate multiphysics effects, including solid and fluid phase phenomena.

3. Computation

One of the primary limitations of diffuse interface methods is the computational cost. By definition, there is a distinct scale separation between the application scale and the diffuse interface scale; indeed, if the scales are not properly separated, the model is unlikely to be accurate. Computationally this presents a challenge, as full resolution of the entire domain is both prohibitively expensive and at the same time unnecessary. Adaptive mesh refinement (AMR) is a computational strategy particularly well suited for diffuse interface methods. Specifically, AMR selectively refines the diffuse interface and coarsens the mesh elsewhere as appropriate. Block-structured AMR (BSAMR) is a particularly attractive type of AMR (Fig. 4). The BSAMR strategy is to divide the domain into distinct levels, each corresponding to a level of refinement,

and then facilitates communication between levels through averaging and interpolation between timesteps. This data structure is particularly advantageous for performance, as the individual patches can easily be divided across a distributed memory computational platform. BSAMR also allows for temporal subcycling, automatically reducing the timestep and increasing the number of iterations on finer levels. This eliminates common CFL difficulties in explicit methods that can arise during mesh refinement.

In this work, we use an in-house code "Alamo" to implement and test the diffuse interface model [57]. Alamo is built on the AMReX library [58], and implements a variety of physical models ranging from fluid mechanics to microstructure evolution. A fully explicit, forward Euler temporal scheme is used to evolve the kinetic equation. The finite difference method is used to compute all spatial derivatives; specifically, a second order central difference stencil is used for the Laplacian of η. . The coarse level timestep is set to 2.5×10^{-5} seconds, and a temporal substep factor of 2 is used between refinement levels, for a finest-level timestep of approximately 2×10^{-8} seconds. Because the governing equation is parabolic, it behaves well when integrated by an explicit solver as long as the timestep is sufficiently small enough to prevent instability. Here, the timestep is chosen to be at least a factor of two smaller than that required by the CFL condition. For more discussion on timestep selection in phase field type models, the reader is referred to [44, 59]. Regridding is set to occur every 100 timesteps (on the coarse level) and occurs whenever the following condition holds:

$$|\nabla \eta| \, |\Delta \boldsymbol{x}| \geq 0.01, \tag{16}$$

where $\Delta \boldsymbol{x}$ is the vector of grid spacings (Fig. 4 left popout). These values are based on previous phase-field type models implemented in Alamo by some of the authors [43, 45, 57, 60], and are checked to ensure that there is no mesh dependency observed in the solution. A full discussion of the regridding methods used by Alamo and AMReX is outside the scope of this work. Instead, the reader is directed to the original AMReX [58] paper, and the associated documentation, and the previously mentioned BSAMR phase field papers for a broader discussion of regridding methods in phase field applications.

Refinement does not currently occur at solid/solid boundaries, unless they intersect the burn interface, in order to maximize performance. The species field ϕ is not evolved in time, but it can still be computationally expensive to calculate. The packed spheres case, for instance, can require significant time to calculate on a highly refined domain, depending on the number of spheres in the system (Eq. (17)). In the BSAMR scheme, ϕ must be either stored at full resolution, or recalculated on-the-fly as domains are refined and coarsened. In the present implementation, ϕ is calculated on the finest level only, and is simply averaged/interpolated elsewhere as the grid evolves. This is acceptable since the evolution of the system always takes place on the finest level only, and is constant elsewhere regardless of the value of ϕ. When plotting the stored value of ϕ, however, it may appear that ϕ is different in the pre-burn and post-burn regions, due to differences in the way it was interpolated. (Fig. 4 right popout).

Table 1: AP, PBAN, HTPB parameters for the solid phase model

Parameter name	**Symbol**	**AP**	**PBAN**	**HTPB**	**AP+ PBAN**	**AP+ HTPB**
Flame speed exponent (-)	n	1.042	0.0	0.0	0.0	0.0
Flame speed coefficient (mm/s)	r	1.222	0.1	0.5	10.01	12.5
Base pressure (MPa)	p_{p}	1.0				
Burned energy (MPa)	w_0	0.0				
Unburned energy (MPa)	w_1	1.0				
Activation energy (MPa)	$w_{1/2}$	2.0				
Diffuse width (mm)	ε	0.0005				
Chemical potential factor (-)	λ	0.001				
Interface energy (MPa)	κ	1.0				
Shape constant (-)	γ	0.02726				

The two-dimensional simulations are generally tractable for a single node or high-performance workstation. All of the 2D simulations presented here were run simultaneously on the STAMPEDE2 supercomputer, with each simulation using a single node with 48 MPI tasks. The time to complete varied between runs, but generally averaged approximately 2 hours of wall-clock computation time for each second of simulation time. The three-dimensional simulations, naturally, required substantially more computational time to complete. The domain size was reduced to 30% of the height of the 2D simulation size to reduce the computational time. The 3D calculations were performed on the INCLINE cluster at the University of Colorado Colorado Springs. Each calculation was run on 4 nodes with 128 processors per node for a total of 512 MPI tasks. The time to complete also varied between runs, but generally averaged approximately 33 hours of wall-clock computation time for each second of simulation time.

4. Results

In this section, we apply the computational phase field model to study a variety of SCP configurations, with the aim of establishing its validity and predictive ability. In this study, we use AP for the oxidizer and consider binders of both PBAN and HTPB. Four different cases are considered: the coupon of pure AP (pure AP); a thin layer of PBAN sandwiched between AP (AP/PBAN sandwich); a thin layer of HTPB sandwiched in between AP (AP/HTPB sandwich); and AP sphere particles with HTPB binder (AP/HTPB packed spheres) in two and three dimensions.

4.1. Pure ammonium perchlorate burning

We begin with a calibration of the model for the pure AP case to established, experimentally measured pressure-dependent AP regression rates. The pressure-dependent mobility is calculated using Eq. (9), and is reported in Table 1 along with parameters used in this work. A simulation domain of $4\,\mathrm{mm} \times 0.5\,\mathrm{mm}$ was used with a base mesh of 16×2 cells and 7 levels of BSAMR refinement. Burn rates are calculated and compared to legacy experimental data reported in [4]. To achieve consistency with experimental measurements, such as those reported in [8, 15, 61], which use a break-wire method to measure burn speed, amounts to measuring the instantaneous effective position of the interface as the location of the leading point of the burn front.

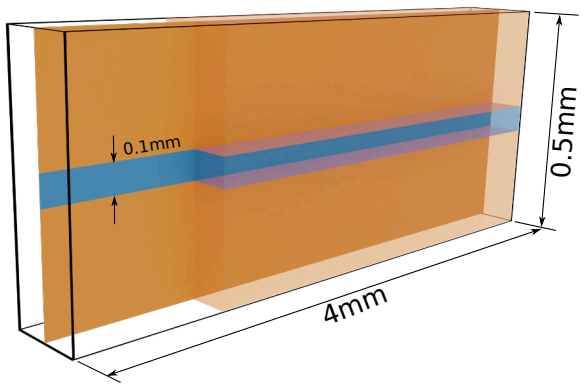

(a) Dimensions of sandwich structure consisting of AP (gold) and HTPB or PBAN binder layer (blue).

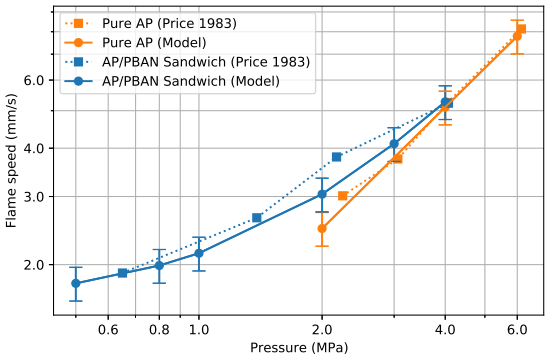

(b) Comparison of model results for flame speed in pure AP and AP+PBAN sandwich structure

Figure 5: AP/PBAN sandwich burn results

Reasonable agreement to experimental values are recovered (Reported in Figs. 5b and 7a). This is unsurprising, given the analytic relation between mobility, chemical potential, and burn rate; nevertheless, it indicates that the model will produce realistic results for this type of monopropellant burn.

4.2. AP and PBAN sandwich

In realistic SCPs, the behavior induced by the SCP geometry (complex interface surface of binder with the packed AP particles) results in complex burn behavior that eludes simplistic analysis. Therefore, to better understand the interactions between oxidizer and binder, sandwich structures provide a simplified yet nontrivial case study. Sandwich structures have been examined in a variety of experimental reports with varied compositions [62–68], over the span of the past several decades. The geometry of sandwich structures is simple: a laminate of binder between two blocks of AP (Fig. 5a). Here, a $4\,\text{mm} \times 0.5\,\text{mm}$ geometry is used with a laminate thickness of 0.1 mm. As with the pure AP case, a 16×2 base grid is used with 7 levels of mesh refinement, and a diffuse interface thickness of $\zeta = 0.015$ is used. Pressures ranging from 500 kPa to 4 MPa are considered, and parameters are adjusted by comparison to the values reported by Price et al. [4].

In this simulation the parameters for AP are held constant with the values that were found for the pure AP combustion and we calibrate the binder parameters only. The resulting burn rate calculations appear to be consistent with experimentally measured values, with an average error of approximately 10% for PBAN, compared to less than 5% for pure AP. (Fig. 5b). Observed variation in the velocity is minimal. The 10% error bars are added to reflect the anticipated uncertainty in the computational results. An interesting point to note is that, although a pressure power law form had been assumed for both the PBAN and mixture regions, the best exponential coefficient was found to be zero, i.e., a constant value was determined to best match the experiments.

A key feature of this model is its ability to capture the complex regression morphology in addition to the regression rate. A comparison was made between experimentally observed burn front shapes (Fig. 6a) and numerical simulation (Fig. 6b). For the numerical results, traces are plotted at every 10 ms; blue traces

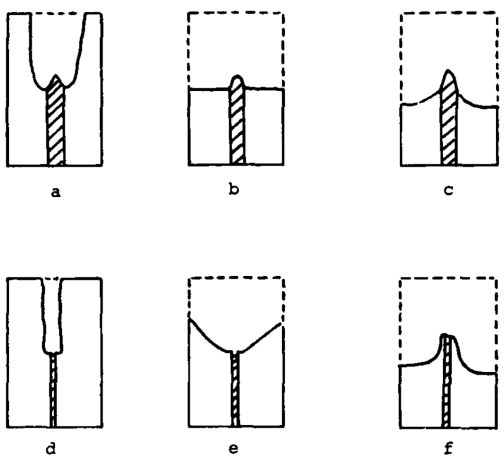

(a) Experimental observations of burn profiles for low pressure (a,d), medium pressure (b,e), and high pressure (e,f); reproduced from Price et al. [4, Fig 1]

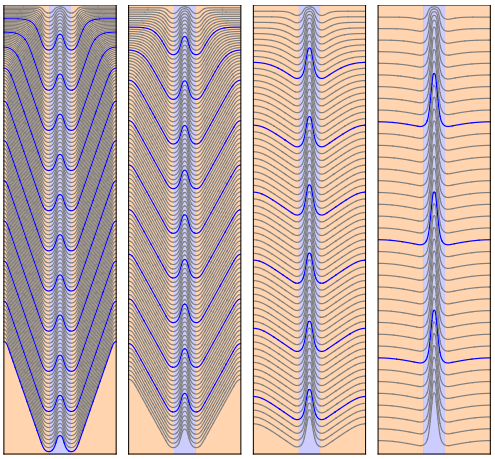

(b) Traces of the burn front evolving over time. Blue traces are plotted at time intervals of $\Delta t = 100\,\text{ms}$. From left to right the pressures are 0.5, 0.8, 2, and 4 MPa.

Figure 6: AP/PBAN Sandwich: comparison between experimentally observed and numerically predicted interface morphology

every 100 ms.

The simulated burn behavior, qualitatively, follows the morphological trends observed in experiments. At low pressures, AP burns very slowly because the pressure is too low to maintain monopropellant burning. This manifests as a deep grooved burn profile, caused by the differential between the burn speeds in the interface region and the pure AP region. Remarkably, we even observe the slight dimple present in the binder layer, which is the result of an excess of binder beyond that which is needed to react locally with AP near the interface. At high pressure, where AP is able to effectively self-react, an opposite trend is observed: the AP burns faster than the binder, leaving a distinctive protrusion of the binder.

4.3. AP and HTPB sandwich

The setup for a sandwich structure composed of AP with an HTPB binder is identical to the AP/PBAN case except for the selection of parameters for the binder and binder interaction. Again, the AP parameters are unchanged. Experimental data from Knott et al. [15] is used for calibration of the binder parameters. It should be noted that we include the experimental data for all binder thickness for comparison from this work, observing that the difference between them is relatively small.

Parameters for HTPB are determined by grid search. As with the PBAN case, it has been determined that the pressure law exponent was negligibly small, meaning that a constant value for the burn rate sufficed to produce the observed results. Comparison to experimental data indicates an approximate error of 5–20% between the simulated regression rate and the observed rate (Fig. 7a). The 10% error bars have been added here as well. It is of interest that an inflection in the burn rate is observed at approximately 8 kPa, matching a similar trend in the experiment. Despite the similar mathematical form to the AP/PBAN case, this demonstrates that nonlinear phenomena can be captured with this model. In this case, we attribute this change to the more extreme morphology at the interface.

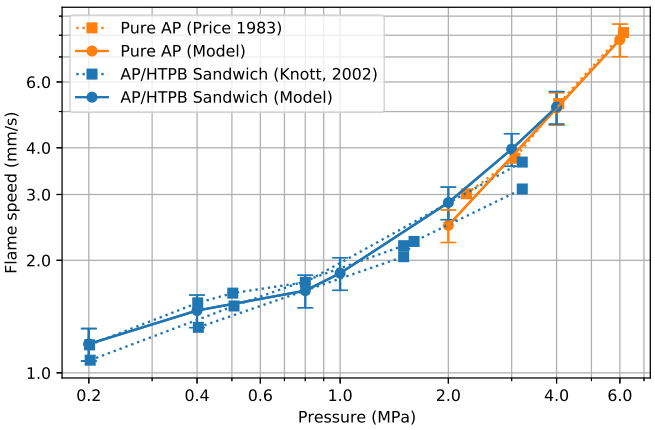

(a) Comparison of model results for flame speed in pure AP and AP+HTPB sandwich structure.

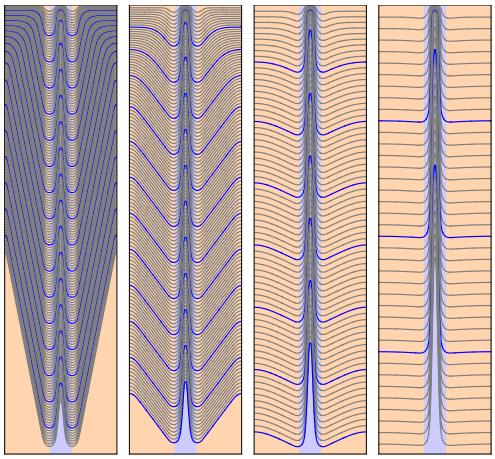

(b) Traces of the burn front evolving over time. Blue traces are plotted at time intervals of $\Delta t = 100\,\text{ms}$. From left to right the pressures are 0.5, 0.8, 2, and 4 MPa.

Figure 7: Regression rates in AP/HTPB sandwich structures with varying pressure

The burn profile is qualitatively similar to that calculated for AP and PBAN (Fig. 7b). In both cases, the interface regresses most quickly at the solid/solid interface, due to the enhanced burn chemistry enabled by the mixing of the binder and AP mass fluxes. As the pressure is increased, the AP matrix is able to sustain a reaction independently. At high enough pressure, the pure AP regression rate exceeds that of the solid/solid interface, essentially leaving a flat AP surface. In all cases, a protrusion formed by the HTPB binder is left behind. At low pressure the binder is quickly consumed, but at high pressure it is persistent. We note that such a protrusion would, in reality, be unstable and unlikely to remain attached as indicated by the model. We expect, however, that the quantity of HTPB not effectively burned would likely correspond to the volume left behind in this model.

4.4. Packed 2D AP spheres in HTPB matrix

In this section we test the predictive capability of the model by considering the practical case of packed AP spheres (with two different mass concentrations) embedded in an HTPB matrix. The initial geometry of the oxidizer particles are modeled as spheres similar to previous studies (Fig. 8a). This test case is representative of practical SCP, and we emphasize that the model parameters are not adjusted to match the results to experimental values; the same parameters determined in the previous sections are used, and the only change in this work is the geometry of the binder and matrix.

The 2D simulation domain is specified to be $4\,\text{mm} \times 1.6\,\text{mm}$ and is packed with spheres having a uniform radial distribution of $r = 55\,\mu\text{m}$. Mass fractions of 78% and 64% AP are considered, which corresponds to volume fractions of 62% and 45%, respectively. In two dimensions, the corresponding area fractions are 74% and 53%, respectively. A 3D mass fraction of 75% was used, instead of 80% as in the corresponding experiment, because of the inherent difficulty in calculating packings with packing factors greater than 62%. Although AP particles are generally irregular, we follow precedent [69] in the use of non-overlapping spheres

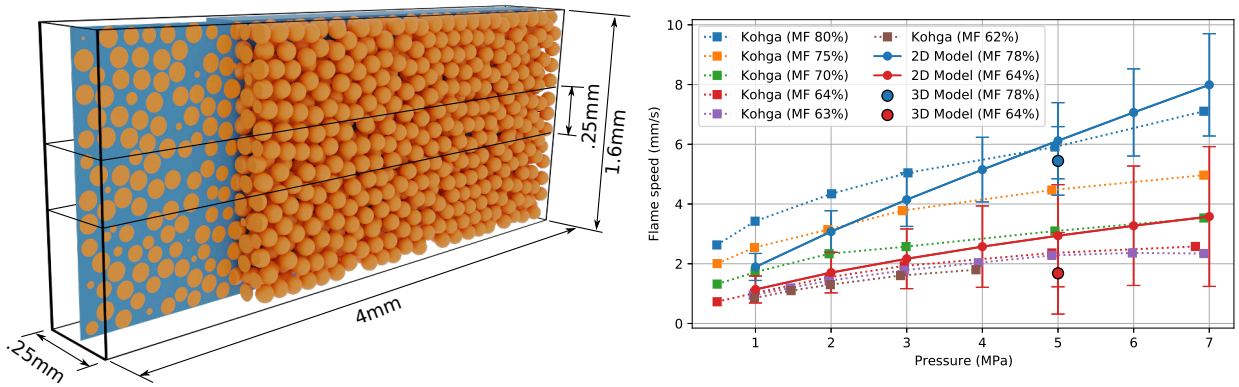

(a) (b)

Figure 8: Results for packed AP spheres in an HTPB matrix. (a) Visualization showing the generated 3D packing and the corresponding 2D slice. The inset 0.25 mm section is the region used for the 3D simulation. (b) Results for the model with mass fractions of 78% and 64%, compared to experimental data reported in [9].

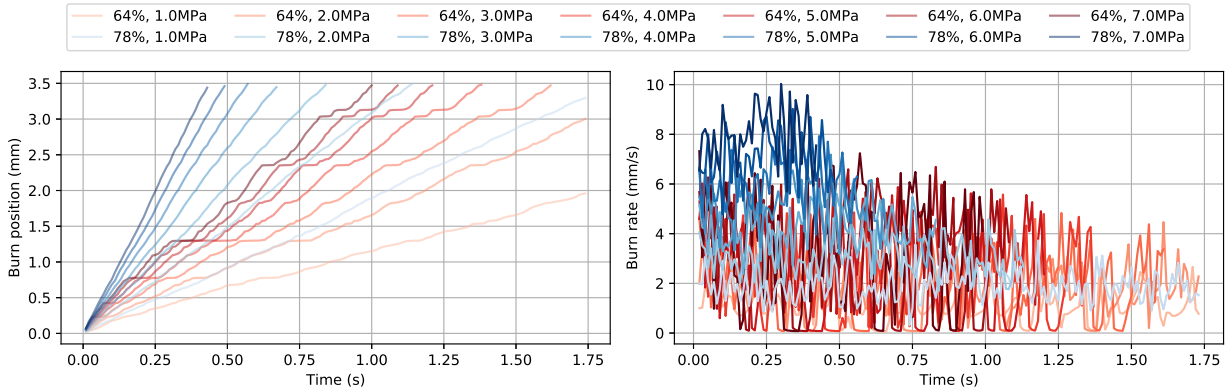

Figure 9: Burn positions (left) and instantaneous interface velocities (right) calculated using central difference

for this calculation. (We note that the effect of non-spherical particles, as well as multi-modal and lognormal radial distributions, is non-trivial; this will constitute future work.) The domain is filled with a unimodal distribution of spheres corresponding to the aforementioned volume fractions. In order to faithfully represent the 3D sample with a 2D model, a 3D domain is packed with spheres using the Jodrey and Tory algorithm [70] implemented in OpenMC [71]. A slice of the 3D spheres in the domain is then used to generate the effective unimodal distribution in 2D. To generate the diffuse species field corresponding for the packed spheres, the formula is used

$$\phi(\boldsymbol{x}) = 1 - \prod_{n=1}^{N} \left\{ \frac{1}{2} + \frac{1}{2} \operatorname{erf}\left[(|\boldsymbol{x} - \boldsymbol{x}_n| - r_n)/\zeta \right] \right\}, \tag{17}$$

where N is the total number of spheres/discs, $\{\boldsymbol{x}_1, \ldots, \boldsymbol{x}_N\}$ are their locations, and $\{r_1, \ldots, r_N\}$ their radii. For the 64% and 75% cases, the number of 2D discs was $N = 426$ and $N = 628$, respectively. The parameter ζ determines the diffusivity of the solid/solid interface ($\zeta \to 0$ recovers the sharp interface limit) and was selected here to be $\zeta = 10\,\mu$m. ($\phi(\boldsymbol{x})$ for the packed spheres is plotted in the right pop-out of Fig. 4.)

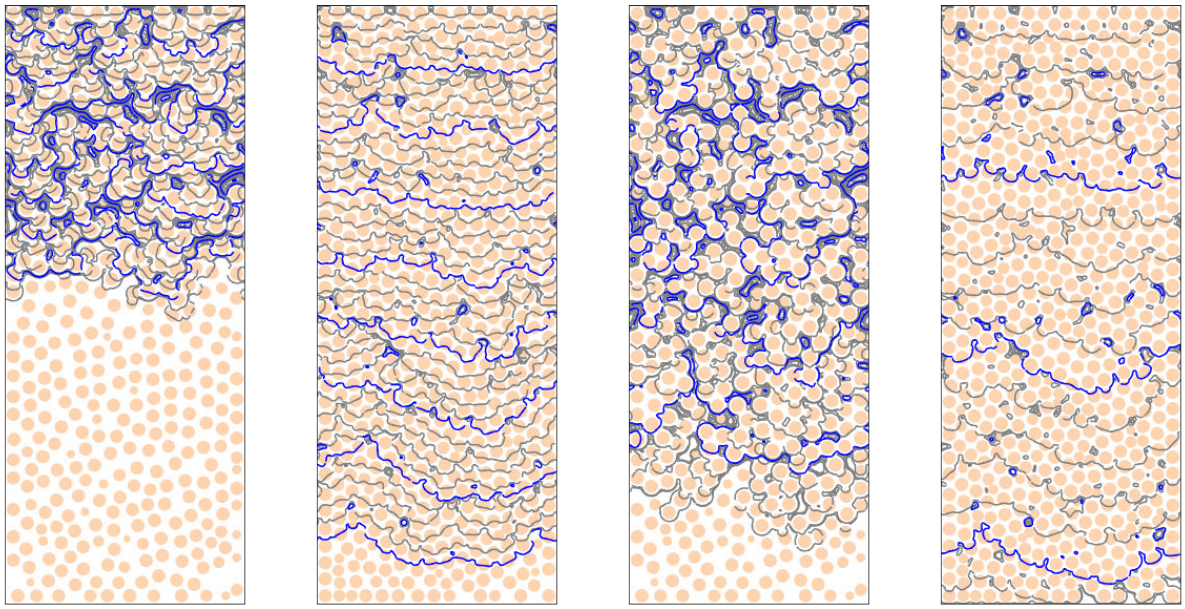

(a) MF = 64%, $p = 1$ MPa (b) MF = 78%, $p = 1$ MPa (c) MF = 64%, $p = 4$ MPa (d) MF = 78%, $p = 4$ MPa

Figure 10: Traces illustrating observed burn front behavior for varying mass fractions and pressures. Gray traces are plotted at intervals of 50 ms, blue traces at intervals of 250 ms.

The burn rate is determined as before by fitting the slope of the effective interface position using linear regression. Unlike with the pure AP or sandwich cases, a substantial amount of variability is observed in the leading point burn location. This is due to the high degree of complexity observed in the burn front, which will be discussed shortly. Simulations have been conducted for pressure from 1–7 MPa at 1 MPa intervals for both volume fractions, and compared to corresponding experimental observations for equivalent SCPs as reported by Kohga [9] (Fig. 8b). The observed error ranges between 5% to 80% error for the 64% mass fraction, and from 1% to 100% for the 70% mass fraction. Errors are calculated based on the RMS difference between between the instantaneous velocity and the approximate velocity, and are represented using error bars. The high degree of variance is a result of the high variability in the instantaneous velocity due to the substantial heterogeneity in the packing. This is clearly observed in the plots of the burn rate position and the calculated velocity vs. time (Fig. 9).

Qualitatively, the results demonstrate marked dependence both on pressure and on concentration, which is well-known to exist. This indicates that the approximations made in the model, despite their simplification of complex burn behavior, do not introduce substantial error. It also shows the predictive power of the model, which is especially apparent here, since the parameters were unchanged from the values obtained in the sandwich calibration tests. (Obviously, a much closer match could be attained if the parameters had been calibrated for this case!) We suggest, therefore, that this model can be used in its present form to investigate the behavior of other types of SCP configurations with reasonable accuracy.

As with the sandwich cases, we also investigate the morphological details of the solid phase regression. Unlike with the previous cases, in which the front approaches a steady-state shape, the randomness of the

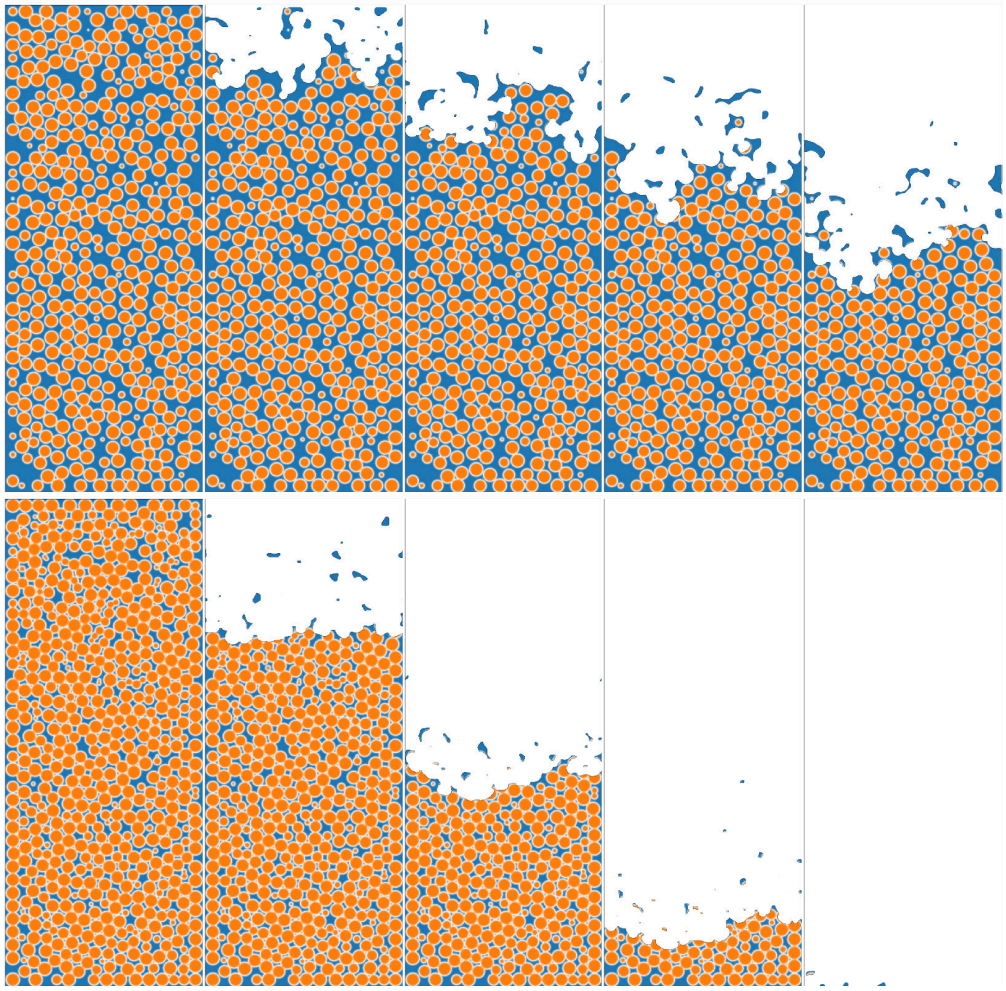

Figure 11: Comparison of burn profiles at $p = 5\,\text{MPa}$ for 64% AP (top) and 78% AP (bottom). Intervals are at $\Delta t = 0.16\,\text{s}$.

the sphere packing induces a highly random and richly complex burn front. Here, we present trace plots illustrating the progression of the burn front in time (Fig. 10). The traces are superimposed on plots of the AP particle locations, and are plotted at 50 ms intervals. The trace diagrams illustrate the qualitative differences between the burn front surface time history.

At constant low pressure, we observe that the morphology of the low concentration AP (Fig. 10a) is substantially more complex than the high concentration case (Fig. 10b). This is unsurprising: low AP concentrations have lower interfacial surface area, and leave large islands of binder that have no AP with which to react. On the other hand, high AP concentrations result in smaller and fewer binder islands, meaning that the majority of the binder is available to react with the AP and there is less binder left behind. A similar trend is observed at high pressure (Figs. 10c and 10d). Trends are also compared for both concentrations at 5 MPa (Fig. 11); here it is clear that, aside from the obvious difference in flame speed, there is a distinct difference in morphology as well as the size and shape of left-behind islands.

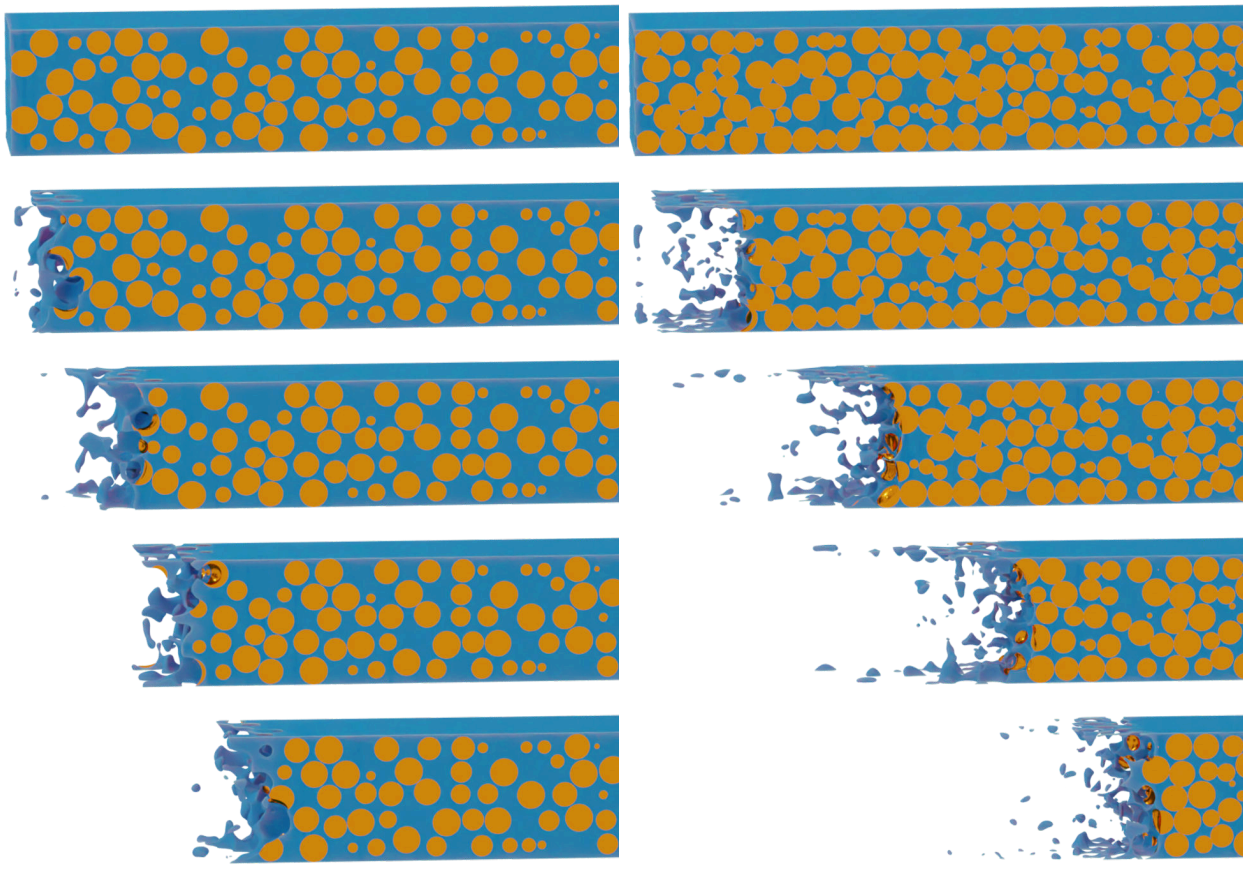

(a) Burn of 64% MF composition at 5 kPa, 180 ms intervals

(b) Burn of 78% MF composition at 5 kPa, 100 ms intervals

Figure 12: 3D simulation of packed AP spheres in HTPB using the diffuse interface method

4.5. 3D AP spheres packed in HTPB matrix

Packed sphere SCP configurations are inherently three-dimensional. As discussed above, 2D simulations cannot faithfully represent a 3D packed sphere structure, as the 3D equivalent of any 2D approximation is an array of packed cylinders, rather than spheres. To determine this effect of dimensionality, 3D simulations have been performed for the $p = 5\,\text{kPa}$ case, for both 64% and 78% AP mass fractions. A simulation domain of 4 mm normal to the burn direction and $0.25\,\text{mm} \times 0.25\,\text{mm}$ in-plane is used, and the same packing configuration is used as that for the corresponding 2D simulations (Fig. 8a). The two faces on the outside of the original domain do not intersect any of the enclosed spheres; the other two include cross-sections of the packed spheres; this allows the simulation to resolve potential edge effects that are only apparent in 3D.

Though not the focus of the work, the process of output visualization is nontrivial and warrants explanation. VisIt [72] is used to perform initial processing of the raw BoxLib output, which entails the calculation of the $\eta \geq 0.5$ isovolume. The geometry is then imported into Blender [73]. Since the raw mesh has varying levels of refinement and does not include full resolution of ϕ it is difficult to visualize the composition. To render the composition over the imported geometry, then, a special shader has been developed by the authors using the open shader language (OSL) to efficiently encode the sphere packing information without

the computational expense of explicitly meshing individual spheres. This allows for surface and volumetric rendering of arbitrary AP/HTPB compositions and geometries using modern rendering techniques. HTPB is rendered using a non-specular semi-transluscent blue shader with subsurface scattering; AP is rendered using an orange, opaque, glossy shader. Each high-resolution 2D render requires approximately 10 seconds on a desktop computer to run.

Burn rate is calculated similarly as for the 2D case. The $\eta = 0.5$ isosurface is calculated for each output file, and the most extreme point in the isosurface is treated as the effective position. It is possible that instantaneous speeds are overestimated (*vis á vis* experimental results) using this method, as a physical trip wire or high-speed imaging may not detect extrema of the burn front morphology that are captured here. It is not expected that this would affect the average burn rate, however, only the variability in the instantaneous burn velocity. Velocity is calculated using the central difference method, and a linear regression is fit to determine average velocity. The variance of the velocity is represented as the error.

For both the 64% and the 78% case, the calculated 3D burn rate is lower than that predicted by the 2D case, although the error between the 3D prediction and the experimental measurement is approximately the same (Fig. 8b). We attribute this difference to two factors. The first, and most significant, is the difference in 2D area fraction vs 3D volume fraction for equivalent packings. As mentioned above, the area fraction is substantially greater than the volume fraction. Therefore, the 3D simulation equivalent to the 2D cases would have a lower interface content, reducing the speed at which the interface regresses. The second factor is the presence of two non-sphere-intersecting faces, which have a lower burn rate due to the locally lower interface content. Upon inspection of the burn front morphology, however, the average curvature of the burn front appears isotropic (i.e., no obvious "bowing out" of the interface between non-sphere-intersecting faces), which indicates that edge effects are negligible.

The morphology of the regressing interfaces qualitatively appears to obey similar trends as that observed in the 2D simulation. The 3D morphology of the unburned ($\eta \geq 0.5$) region is visualized at 180 ms intervals for the 64% case and 100 ms for the 78% case. (Different intervals are used to allow for better qualitative comparison of the interface.) For the 64% case, the interface moves more slowly, as its motion is hampered by large binder peninsulas. The burn progresses via rapid jumps forward as the surface encounters AP and solid/solid interface regions, and otherwise moves slowly. The burn leaves behind large islands of binder that would normally be advected away by the flow. The burn progresses quickly in the 78% case and is rarely slowed substantially by binder obstacles because of the large AP concentration. This simulation shows that more islands of binder are left behind. Although they are more numerous, the islands are substantially smaller than those in the 64% case. It should be emphasized that these islands are not "ejected" from the interface but merely left behind. The apparent trail of islands is thus the result of the greater speed of the interface. In both cases, since a greater concentration of islands that are located at the non-sphere-intersecting faces, the effects of edges are significant in 3D simulations.

5. Conclusion

In this work, we present a solid-phase model for calculating the burn rate and morphology for solid composite propellants using a diffuse interface method. The model is based on classic work from phase field theory, which allows for the thermodynamics of the system to be captured faithfully in a geometrically arbitrary setting. We demonstrate the interpretability between the model parameters and physical values, by showing the relationship between free energy, mobility, interface shape, and flame speed. We then develop a scheme for reduced-order modeling of the effect of interface mixing on the burn rate, using a heuristic combustion model and diffuse species field parameter field.

The model is applied to a selection of experimentally verifiable SCPs. It is first calibrated to AP monopropellant burn by comparison to legacy data. Sandwich structures with both PBAN and HTPB binders are then used to calibrate the binder model parameters for a range of pressures. Finally, the model is applied predictively (i.e., without adjusting parameters) to study packed AP spheres in an HTPB matrix at varying mass concentrations and varying pressures. For the sandwich cases, against which the model was calibrated, the error was observed to be 10% or less in most cases. For the predictive packed spheres case, the error is more substantial in some cases (up to 100%) but was less than 10% for the 64% case and when $p = 5\,\mathrm{MPa}$ for both packings. Further development and calibration of the model will focus on increasing its predictive capacity for these and other SCP configurations. Future work will also require validation of the model against other experimental datasets, considering broader and more realistic configurations, including the Miller packings [74], that have served as a benchmark for validation in other computational modeling efforts [75–77]. An important conclusion that can be drawn from this work, regarding solid phase models of this type, is that it is necessary to explicitly account for interface content. In other words, it is an oversimplification to simply rely on individual decomposition/burn rates; to do so will inevitably fail to capture the increased burn rate observed in SCPs burning below 1 MPa. It is also important to reiterate the connection between pressure, concentration, and islands of left-behind binder, which may have important implications for unburned binder and combustion efficiency.

We have proposed a highly reduced-order model intended to capture the burn rate and morphology of SCPs, and we caution that care should be taken in the interpretation and extension of the model results. The primary simplification is the approximation of the mobility, L, using a pressure and species dependent power law. In reality, L should be understood to depend primarily on temperature, which is determined by the heat flux, which is determined by the reaction chemistry, which is dependent on the mass flux, which in turn is dependent on the mobility.

Though the proposed formulation includes several order-reducing simplifications, and is apparently able to make some predictions with them, the real power of the phase field approach lies in its ability to robustly integrate multiphysics phenomena. Specifically, in the solid phase, the use of continuous η and ϕ fields allow for the "phasing in" of solid-phase governing equations to model thermal transport and thermoelastic response. In fact, a robust theory has already been developed for imposing boundary conditions over diffuse

phase field boundaries [78], and elastic solvers have already been implemented with those capabilities [43, 45, 57] to simulate mechanics; all these lay the groundwork for future expansion of the model. Of greater consequence, however, is the resolution of the fluid phase—essential to capturing behavior such as detailed flame locations, heat flux back to the solid, and erosive burning [79]—which is not present in the current model. We refer the reader to current work by some of the authors that presents a method for robust coupling of solid and fluid phases across a diffuse deflagrating boundary [51], which will provide the basis for concurrent simulations of the solid and gas phase.

Acknowledgments

BK and BR were supported by the Office of Naval Research [grant number #N00014-21-1-2113]. MQ was supported in this effort by UCCS Department of Mechanical and Aerospace Engineering start-up funds. This work used the INCLINE cluster at the University of Colorado Colorado Springs. INCLINE is supported by the National Science Foundation, Grant #2017917. This work also used the Extreme Science and Engineering Discovery Environment (XSEDE) on the STAMPEDE2 supercomputer at the Texas Advanced Computing Center (TACC) through allocation TG-PHY130007; XSEDE is supported by the National Science Foundation [grant number ACI-1548562]. Finally, the authors gratefully acknowledge many discussions with Dr. Brian Bojko that substantially strengthened this work.

References

[1] G. R. Morrow, E. L. Petersen, The effects of ap particle size and concentration on ap/htpb composite propellant burning rates, in: 55th AIAA Aerospace Sciences Meeting, 2017, p. 0831.

[2] E. K. Bastress, Modification of the burning rates of ammonium perchlorate solid propellants by particle size control, Ph.D. thesis, Princeton University (1961).

[3] L. Shannon, Modification of the burning rates of ammonium perchlorate solid propellants by particle size control, PhD Thesis,University of California, Berkeley (1963).

[4] E. W. Price, J. Sambamurthi, R. Panyam, R. K. Sigman, Combustion of ammonium perchlorate-polymer sandwiches, Tech. rep., Georgia Institute of Technology School of Aerospace Engineering (1983).

[5] T. Boggs, Deflagration rate, surface structure, and subsurface profile of self-deflagrating single crystals of ammonium perchlorate, AIAA J. 8 (1970) 867–873.

[6] J. B. Levy, R. Friedman, Further studies of pure ammonium perchlorate deflagration, in: Symposium (International) on Combustion, Vol. 8, Elsevier, 1961, p. 663–672.

[7] D. Watt Jr, E. Petersen, The deflagration of single crystals of ammonium perchlorate, Combust. Flame 14 (1970) 297–302.

[8] S. Hayakawa, C. Nakao, M. Tanaka, An effect of oxidizer particle size on combustion stability in composite propellants, in: 36th AIAA/ASME/SAE/ASEE Joint Propulsion Conference and Exhibit, 2000, 2000-3700.

[9] M. Kohga, Burning characteristics and thermochemical behavior of ap/htpb composite propellant using coarse and fine ap particles, Propellants Explos. Pyrotech. 36 (2011) 57–64.

[10] B. Crawford, C. Huggett, F. Daniels, R. Wilfong, Direct determination of burning rates of propellant powders, Anal. Chem. 19 (1947) 630–633.

[11] N. Eisenreich, H. Kugler, F. Sinn, An optical system for measuring the burning rate of solid propellant strands, Propellants Explos. Pyrotech. 12 (1987) 78–80.

[12] H. Rezaiguia, P.-J. Liu, Flame response of solid laminate propellant ap/htpb to pressure perturbations, in: 2016 7th International Conference on Mechanical and Aerospace Engineering (ICMAE), IEEE, 2016, p. 185–190.

[13] A. Atwood, T. Boggs, P. Curran, T. Parr, D. Hanson-Parr, C. Price, J. Wiknich, Burning rate of solid propellant ingredients, part 1: Pressure and initial temperature effects, J. Propul. Power 15 (1999) 740–747.

[14] A. Atwood, T. Boggs, P. Curran, T. Parr, D. Hanson-Parr, C. Price, J. Wiknich, Burning rate of solid propellant ingredients, part 2: Determination of burning rate temperature sensitivity, J. Propul. Power 15 (1999) 748–752.

[15] G. Knott, M. Brewster, Modeling the combustion of propellant sandwiches, Combust. Sci. Technol. 174 (2002) 61–90.

[16] W. Strahle, J. Handley, T. Milkie, Catalytic effects in the combustion of ap-htpb sandwiches to 3200 psia, Combust. Sci. Technol. 8 (1973) 297–304.

[17] M. Summerfield, Burning mechanism of ammonium perchlorate propellants, Solid Propellant Rocket Research (1960) 141–182.

[18] C. Hermance, A detailed model of the combustion of composite solid propellants, in: 2nd Solid Propulsion Conference, 1967, p. 1511.

[19] M. W. Beckstead, R. Derr, C. Price, A model of composite solid-propellant combustion based on multiple flames, AIAA J. 8 (1970) 2200–2207.

[20] R. Glick, Steady-state combustion of nonmetallized composite solid propellant, Tech. rep., Morton Thiokol, Inc. (1975).

[21] N. S. Cohen, L. D. Strand, An improved model for the combustion of ap composite propellants, Aiaa J. 20 (1982) 1739–1746.

[22] S. Isert, S. F. Son, The relationship between flame structure and burning rate for ammonium perchlorate composite propellants, in: Energetic Materials, Springer, 2017, p. 171–211.

[23] M. L. Gross, M. W. Beckstead, Steady-state combustion mechanisms of ammonium perchlorate composite propellants, J. Propul. Power 27 (2011) 1064–1078.

[24] B. T. Bojko, M. Gross, T. L. Jackson, Investigating dimensional effects on predicting burning rates of heterogeneous solid propellants, in: AIAA Scitech 2019 Forum, 2019, 2019-1240.

[25] M. King, Model for steady-state combustion of unimodal composite solid propellants, in: 16th Aerospace Sciences Meeting, 1978, 1978-216.

[26] W. Cai, P. Thakre, V. Yang, A model of ap/htpb composite propellant combustion in rocket-motor environments, Combust. Sci. Technol. 180 (2008) 2143–2169.

[27] J. Renie, J. Condon, J. Osborn, Oxidizer size distribution effects on propellant combustion, Aiaa J. 17 (1979) 877–883.

[28] C. Price, T. Boggs, R. Derr, The steady-state combustion behavior of ammonium perchlorate and cyclotetramethylenetetranitramine, in: 17th Aerospace Sciences Meeting, 1979, 1979-164.

[29] J. C. Thomas, G. R. Morrow, C. A. Dillier, E. L. Petersen, Comprehensive study of ammonium perchlorate particle size/concentration effects on propellant combustion, J. Propul. Power 36 (2020) 95–100.

[30] M. L. Gross, T. D. Hedman, Towards the simplified composite propellant burning rate model based on detailed chemistry calculations, International Journal of Energetic Materials and Chemical Propulsion 14 (2015).

[31] H. Wang, D. J. Kline, M. R. Zachariah, In-operando high-speed microscopy and thermometry of reaction propagation and sintering in a nanocomposite, Nat. Commun. 10 (2019) 1–8.

[32] V. Babuk, V. Vasilyev, V. Sviridov, Formation of condensed combustion products at the burning surface of solid rocket propellant, Progress in Astronautics and Aeronautics Series 185 (2000) 749–776.

[33] A. Hegab, T. Jackson, J. Buckmaster, D. S. Stewart, Nonsteady burning of periodic sandwich propellants with complete coupling between the solid and gas phases, Combust. Flame 125 (2001) 1055–1070.

[34] L. Massa, T. Jackson, M. Short, Numerical solution of three-dimensional heterogeneous solid propellants, Combust. Theor. Model. 7 (2003) 579.

[35] T. Kumar, T. L. Jackson, Three-dimensional thermo-mechanical simulations of heterogeneous solid propellants, Combust. Flame 233 (2021) 111590.

[36] X. Wang, T. Jackson, L. Massa, Numerical simulation of heterogeneous propellant combustion by a level set method, Combust. Theor. Model. 8 (2004) 227–254.

[37] Z.-W. Ye, Y.-G. Yu, Numerical simulation and unsteady combustion model of ap/htpb propellant under depressurization by rotation, Propellants Explos. Pyrotech. 44 (2019) 493–504.

[38] T. Kumar, C. H. Rycroft, T. L. Jackson, Eulerian thermo-mechanical simulations of heterogeneous solid propellants using an approximate projection method, Combust. Flame 219 (2020) 198–211.

[39] D. S. Stewart, G. A. Ruderman, J. J.-i. Yoh, A thermomechanical model for energetic materials with phase transformations: analysis of simple motions, SIAM J. Appl. Math. 63 (2003) 538–563.

[40] D. S. Stewart, G. A. Ruderman, J. J.-i. Yoh, A thermomechanical model for energetic materials with phase transformations, SIAM J. Appl. Math. 63 (2003) 510–537.

[41] D. S. Stewart, K. Lee, Modeling the thermo-mechanical-chemical behavior of condensed phase reactive materials, Propellants Explos. Pyrotech. 45 (2020) 270–283.

[42] L.-Q. Chen, Phase-field models for microstructure evolution, Annu. Rev. Mater. Res. 32 (2002) 113–140.

[43] M. Goklui, B. Runnels, Multiphase field modeling of grain boundary migration mediated by emergent disconnections, Acta Mater. 217 (2021) 117149.

[44] N. Moelans, B. Blanpain, P. Wollants, An introduction to phase-field modeling of microstructure evolution, Calphad 32 (2008) 268–294.

[45] V. Agrawal, B. Runnels, Block structured adaptive mesh refinement and strong form elasticity approach to phase field fracture with applications to delamination, crack branching and crack deflection, Comput. Method. Appl. M. 385 (2021) 114011.

[46] T. Wang, X. Ye, Z. Liu, X. Liu, D. Chu, Z. Zhuang, A phase-field model of thermo-elastic coupled brittle fracture with explicit time integration, Comput. Mech. 65 (2020) 1305–1321.

[47] L. Rátkai, T. Pusztai, L. Gránásy, Phase-field lattice boltzmann model for dendrites growing and moving in melt flow, npj Comput. Mater. 5 (2019) 1–10.

[48] N. Favrie, S. L. Gavrilyuk, R. Saurel, Solid–fluid diffuse interface model in cases of extreme deformations, J. Comput. Phys. 228 (2009) 6037–6077.

[49] D. M. Anderson, G. B. McFadden, A. A. Wheeler, Diffuse-interface methods in fluid mechanics, Annu Rev Fluid Mech 30 (1998) 139–165.

[50] C.-Y. Zhang, H. Ding, P. Gao, Y.-L. Wu, Diffuse interface simulation of ternary fluids in contact with solid, J. Comput. Phys. 309 (2016) 37–51.

[51] E. M. Schmidt, M. J. Quinlan, B. Runnels, A model for diffuse solid-fluid phase-boundary driven flow (2022).

[52] L. D. Landau, V. L. Ginzburg, On the theory of superconductivity, Zh. Eksp. Teor. Fiz. 20 (1950) 1064.

[53] G. Caginalp, P. Fife, Phase-field methods for interfacial boundaries, Physical Review B 33 (11) (1986) 7792.

[54] J. Langer, Models of pattern formation in first-order phase transitions, in: Directions in condensed matter physics: memorial volume in honor of Shang-Keng Ma, World Scientific, 1986, pp. 165–186.

[55] R. Ye, Y.-g. Yu, Y.-j. Cao, Analysis of micro-scale flame structure of ap/htpb base bleed propellant combustion, Defence Technology 9 (2013) 217–223.

[56] M. Chen, J. Buckmaster, T. Jackson, L. Massa, Homogenization issues and the combustion of heterogeneous solid propellants, Proceedings of the Combustion Institute 29 (2) (2002) 2923–2929.

[57] B. Runnels, V. Agrawal, W. Zhang, A. Almgren, Massively parallel finite difference elasticity using block-structured adaptive mesh refinement with a geometric multigrid solver, J. Comput. Phys. 427 (2021) 110065.

[58] W. Zhang, A. Almgren, V. Beckner, J. Bell, J. Blaschke, C. Chan, M. Day, B. Friesen, K. Gott, D. Graves, et al., Amrex: a framework for block-structured adaptive mesh refinement, Journal of Open Source Software 4 (2019) 1370–1370.

[59] A. Vondrous, M. Selzer, J. Hötzer, B. Nestler, Parallel computing for phase-field models, The International journal of high performance computing applications 28 (1) (2014) 61–72.

[60] E. Eren, B. Runnels, J. Mason, Evolution of interfaces, triple points, and quadruple points using discrete interface equations of motion, arXiv preprint arXiv:2203.03167 (2022).

[61] E. W. Price, J. Sambamurthi, R. Panyam, R. K. Sigman, Combustion of ammonium perchlorate-polymer sandwiches, Tech. rep., Georgia Institute Of Technology School Of Aerospace Engineering (1984).

[62] B. Ermolaev, A. Korotkov, Y. V. Frolov, Laws of combustion of a solid-propellant sandwich, Combustion, Explosion and Shock Waves 6 (1970) 251–257.

[63] B. Chorpening, M. Brewster, Emission imaging of ap/htpb propellant sandwich combustion, Combust. Sci. Technol. 174 (2002) 39–60.

[64] S. R. Chakravarthy, E. W. Price, R. K. Sigman, J. M. Seitzman, Plateau burning behavior of ammonium perchlorate sandwiches and propellants at elevated pressures, J. Propul. Power 19 (2003) 56–65.

[65] S. R. Chakravarthy, J. M. Seitzman, E. W. Price, R. K. Sigman, Intermittent burning of ammonium perchlorate-hydrocarbon binder monomodal matrixes, sandwiches, and propellants, J. Propul. Power 20 (2004) 101–109.

[66] K. Ishitha, P. Ramakrishna, Studies on the role of iron oxide and copper chromite in solid propellant combustion, Combust. Flame 161 (2014) 2717–2728.

[67] K. Gnanaprakash, S. R. Chakravarthy, R. Sarathi, Combustion mechanism of composite solid propellant sandwiches containing nano-aluminium, Combust. Flame 182 (2017) 64–75.

[68] K. Gnanaprakash, S. Chakravarthy, Effect of binder melt flow on the leading edge flames of solid propellant sandwiches, Proc. Combust. Inst. 37 (2019) 3127–3134.

[69] C. Dennis, B. Bojko, On the combustion of heterogeneous ap/htpb composite propellants: A review, Fuel 254 (2019) 115646.

[70] W. Jodrey, E. Tory, Computer simulation of close random packing of equal spheres, Phys. Rev. A 32 (1985) 2347.

[71] P. K. Romano, N. E. Horelik, B. R. Herman, A. G. Nelson, B. Forget, K. Smith, Openmc: A state-of-the-art monte carlo code for research and development, Ann. Nucl. Energy 82 (2015) 90–97.

[72] H. Childs, E. Brugger, B. Whitlock, J. Meredith, S. Ahern, D. Pugmire, K. Biagas, M. Miller, C. Harrison, G. H. Weber, H. Krishnan, T. Fogal, A. Sanderson, C. Garth, E. W. Bethel, D. Camp, O. Rübel, M. Durant, J. M. Favre, P. Navrátil, Visit: An end-user tool for visualizing and analyzing very large data, in: High Performance Visualization–Enabling Extreme-Scale Scientific Insight, 2012, pp. 357–372. doi:10.1201/b12985.

[73] Blender Online Community, Blender - a 3D modelling and rendering package, Blender Foundation, Blender Institute, Amsterdam (2022).
URL http://www.blender.org

[74] R. Miller, Effects of particle size on reduced smoke propellant ballistics, in: 18th Joint Propulsion Conference, 1982, p. 1096.

[75] J. Buckmaster, T. Jackson, M. Ulrich, Numerical modeling of heterogeneous propellant combustion, in: 37th Joint Propulsion Conference and Exhibit, 2001, p. 3579.

[76] J. Buckmaster, T. Jackson, A. Hegab, S. Kochevets, M. Ulrich, Randomly packed heterogeneous propellants and the flames they support, in: 39th Aerospace Sciences Meeting and Exhibit, 2001, p. 337.

[77] K. C. Brown, V. Sankaran, T. L. Jackson, Mesoscale modeling of solid propellant burn rates, in: AIAA Scitech 2019 Forum, 2019, p. 1236.

[78] H.-C. Yu, H.-Y. Chen, K. Thornton, Extended smoothed boundary method for solving partial differential equations with general boundary conditions on complex boundaries, Modelling and Simulation in Materials Science and Engineering 20 (7) (2012) 075008.

[79] A. Isfahani, J. Zhang, T. Jackson, Erosive burning of homogeneous and heterogeneous solid propellants, in: 45th AIAA/ASME/SAE/ASEE Joint Propulsion Conference & Exhibit, 2009, p. 5498.